Journal of Nuclear Materials 396 (2010) 272–282

Contents lists available at ScienceDirect

Journal of Nuclear Materials

journal homepage: www.elsevier.com/locate/jnucmat

Modeling of thermo-mechanical and irradiation behavior of mixed oxide fuel for sodium fast reactors

Aydın Karahan *, Jacopo Buongiorno

Center for Advanced Nuclear Energy Systems, Nuclear Science and Engineering Department, Massachusetts Institute of Technology, MA, United States

ARTICLE INFO

Article history:
Received 20 October 2009
Accepted 23 November 2009

ABSTRACT

An engineering code to model the irradiation behavior of UO_2—PuO_2 mixed oxide fuel pins in sodium-cooled fast reactors was developed. The code was named fuel engineering and structural analysis tool (FEAST-OXIDE). FEAST-OXIDE has several modules working in coupled form with an explicit numerical algorithm. These modules describe: (1) fission gas release and swelling, (2) fuel chemistry and restructuring, (3) temperature distribution, (4) fuel–clad chemical interaction and (5) fuel–clad mechanical analysis. Given the fuel pin geometry, composition and irradiation history, FEAST-OXIDE can analyze fuel and cladding thermo-mechanical behavior at both steady-state and design-basis transient scenarios. The code was written in FORTRAN-90 program language. The mechanical analysis module implements the LIFE algorithm. Fission gas release and swelling behavior is described by the OGRES and NEFIG models. However, the original OGRES model has been extended to include the effects of joint oxide gain (JOG) formation on fission gas release and swelling. A detailed fuel chemistry model has been included to describe the cesium radial migration and JOG formation, oxygen and plutonium radial distribution and the axial migration of cesium. The fuel restructuring model includes the effects of as-fabricated porosity migration, irradiation-induced fuel densification, grain growth, hot pressing and fuel cracking and relocation. Finally, a kinetics model is included to predict the clad wastage formation. FEAST-OXIDE predictions have been compared to the available FFTF, EBR-II and JOYO databases, as well as the LIFE-4 code predictions. The agreement was found to be satisfactory for steady-state and slow-ramp over-power accidents.

1. Introduction

Sodium-cooled Fast Reactors (SFR) have regained worldwide interest in recent years thanks to international programs such as Generation-IV [1] and the Global Nuclear Energy Partnership (GNEP) [2]. The success of these reactors in accomplishing their mission of energy production and improved actinide management, while attaining competitive economics, will largely depend upon the ability of their fuel to operate reliably at high burnup, power density and plant thermal efficiency. The primary fuel candidates for sodium fast reactors are oxide and metal fuels. Although the metal fuel has many advantages, its poor compatibility with the stainless steel clad at high temperatures limits the plant thermal efficiency and also the performance of the fuel in long transient scenarios [3]. The oxide fuel has been widely used in the world in light water reactors, fast reactors and gas cooled reactors. Its maturity and ease of fabrication make it a very attractive candidate for future nuclear systems. First, the oxide fuel has good chemical stability with the stainless steel clad at high temperatures (~700 °C). It is possible to control the fuel–clad chemical interaction by adjusting the initial oxygen-to-metal ratio of the fuel. Its high melting temperature is also advantageous. However, a significant part of the fuel operates below the half of the melting point. As a consequence, the fuel is rather stiff and fuel–clad mechanical interaction (FCMI) becomes a life limiting issue, especially for the transient over-power scenarios. Developing irradiation and thermal creep and void swelling resistant cladding materials such as oxide dispersion strengthened ferritic/martensitic stainless steel [4], may enable operation at higher temperature and burnup, thus rendering oxide fuel quite promising for sodium fast reactor systems.

The objective of this work was to develop a robust and reliable code, which was called fuel engineering and structural analysis tool (FEAST-OXIDE), to model the irradiation behavior of UO_2–PuO_2 mixed oxide fuel pins in sodium-cooled fast reactors for the steady-state and design-basis accident scenarios. In FEAST-OXIDE the fuel and cladding regions can be divided into up to eight radial nodes each; however, six radial nodes in the fuel region and three radial nodes within the cladding region are recommended as optimum. Axial nodes are also user specified. A maximum of 20 axial nodes is allowed. The user must specify the fuel pin geometry, composition and operating conditions (coolant inlet temperature

* Corresponding author. Tel.: +1 617 258 0752.
E-mail address: karahan@mit.edu (A. Karahan).

0022-3115/$ - see front matter © 2009 Elsevier B.V. All rights reserved.
doi:10.1016/j.jnucmat.2009.11.021

and mass flow rate, and axial power distribution, fast neutron flux, flux to dose conversion factor); for transients, the transient starting time and the operating conditions throughout the event must also be specified by the user. The code implements an explicit numerical algorithm and couples the models describing the relevant physical phenomena. A schematic view of the code structure is given in Fig. 1. The Gauss–Jordan matrix solver algorithm [5] was adopted to solve the mechanical equilibrium equation and the heat equation. FEAST-OXIDE includes all the known important phenomena of the mixed oxide fuel for the fast reactor conditions with mechanistic approaches whenever possible.

The main modules of FEAST-OXIDE are briefly described in Sections 2–6; the validation effort is discussed in Section 7. The conclusions are provided in Section 8. A detailed description of FEAST-OXIDE can be found in [6].

2. Fission gas release and swelling

The operational gas release and swelling (OGRES) developed at Harwell is a mature model based on 20 year experimental and theoretical work (1960s–1980s) [7–9]. It is incorporated into FEAST-OXIDE to simulate the behavior of fission gases. The model treats intra-granular and intergranular gas behavior, separately. The intra-granular model describes the gas release to the grain boundary and the behavior of the intra-granular bubbles. It superimposes all the relevant processes onto a system with one representative bubble size. This has the advantage of retaining the correct physical representation while producing a model that is sufficiently fast for use in larger fuel codes. Intra-granular model is augmented with Non-Equilibrium FIssion Gas (NEFIG) model to describe the behavior of intra-granular gas in case of rapid heating

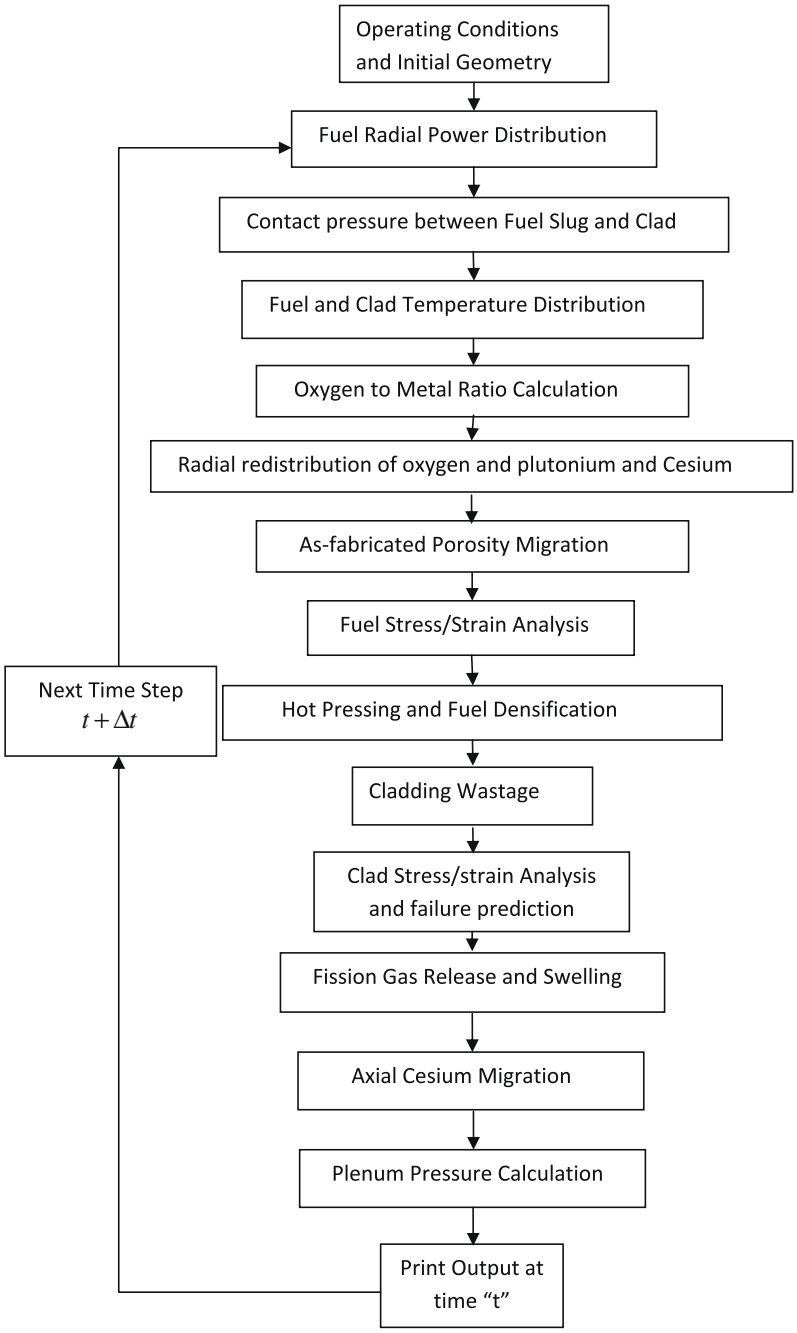

Fig. 1. Flow sheet of FEAST-OXIDE.

scenarios [10]. The intergranular, or grain boundary model describes the swelling behavior of grain boundary bubbles, interlinkage and release to the fuel pin free volume. It is a sophisticated model because: (1) grain edge and face porosity are modeled separately, (2) partitioning of the gas between the faces and edges and its effect on release from the grains, as well as gas transfer between edge and face bubbles are modeled, (3) dynamics of vacancy flow on the grain boundaries are included.

2.1. Intra-granular gas model

The intra-granular gas model (OGRES-I) is a rate theory approach [7,8]. It deals with four processes: nucleation of bubbles on vacancy clusters in fission tracks; complete destruction of bubbles by fission spikes; diffusion of gas from the interior of the fuel grains to the grain boundaries; and bubble movement towards the grain boundary under the temperature gradient driving force (only above 1600 °C). The equation set given in [7,8] for gas atoms in the matrix, intra-granular gas are simultaneously solved with finite-difference approach by dividing the grain into 15 radial nodes. The equation of state of fission gases is modeled with Carnahan–Starling hard sphere model [11]. Note that, unlike Booth's approach [12], the algorithm tracks the intra-granular bubbles as a function of time. Although the swelling due to intra-granular gas bubbles is small under normal operating conditions, it can be considerably high in case of rapid heating transients; hence, the steady-state predictions provide the initial conditions for the transient intra-granular gas model.

2.1.1. Gas diffusion coefficient

The trap free gas diffusion coefficient is given as a function of temperature and thermal rating (specific power) [13]. The thermal rating reflects the enhancement due to fission. The fission-enhanced diffusion becomes significant at temperatures below half of the melting point.

$$D_g = 7.6\times10^{-10}\exp\left(-\frac{35000}{T}\right) + \left[2.3\times10^{-20}\exp\left(-\frac{15000}{T}\right)+3\times10^{-26}\right]R \quad (1)$$

D_g is the gas diffusion coefficient (m^2/s), R is the rating (W/kg), T is the temperature (K).

In this study, Eq. (1) is modified if the joint oxide gain (JOG) forms at the fuel surface (see Section 3). The formation of JOG and resulting intense diffusion of fission products and internal stresses generated in the fuel results in trans-granular cracking of the grains. Hence, reduced grain size may lead to a higher fission gas release rate at the brittle peripheral region of the fuel [14]. To account for the effect of JOG on the fission gas release, the temperature independent part of the gas diffusion coefficient (second term in the bracket in Eq. (1)) has been increased to match the low temperature fission gas release behavior reported in Ref. [9] (see Section 2.4):

$$D_g = 7.6\times10^{-10}\exp\left(-\frac{35000}{T}\right) + \left[2.3\times10^{-20}\exp\left(-\frac{15000}{T}\right)+5\times10^{-25}\right]R \quad (2)$$

2.1.2. NEFIG model

NEFIG simulates the behavior of fission gases and intra-granular gas bubbles in case of rapid heating accidents [10]. It is activated when the fuel temperature locally exceeds 1800 °C [15]. The model is based on vacancy flow. It follows the transfer of gas from solution into gas bubbles; the coalescence of the bubbles arising from their uni-directional drift in a temperature gradient; the change in bubble radius arising from bubble coalescence, the time-dependent acquisition of vacancies from the grain boundaries and the release of gas in the form of gas bubbles. Consistently with OGRES-I, the bubble population is represented by a single bubble size. The dissolved gas concentration decreases with time due to: (1) pick-up of single gas atoms by bubbles migrating under the influence of a temperature gradient driving force, and (2) the collection of single gas atoms into the bubbles by both gas atom and bubble random motion.

2.2. Grain boundary gas behavior

When the gas is released from the fuel grains, it collects initially at the grain boundaries before being released to the pin free volume. It is generally accepted [15] that the major process leading to gas release is the growth and subsequent inter-linkage of grain boundary bubbles for a typical sodium fast reactor operating condition. Experimental evidence shows that interconnected channels exist along the edges of grains after relatively modest burn-ups and temperatures, and that these can permit continuous gas release [15].

The model geometry suggested for the edge and face bubbles in Ref. [9] is adopted in this study. The gas accumulates on the grain faces and edges by diffusion from the grain interior and its division between the face and edge porosity, causing the edge and face bubbles to grow and later interlink. Interaction and competition between edge and face porosity during their growth is described by emission and absorption of vacancies on the grain boundary. The driving force is the difference in chemical potential for vacancies between the cavity surface and the grain boundary. Note that in the original OGRES-II [9] model the chemical potential is defined for stress free conditions. In this work, the stress on the grain boundary bubbles is accounted as follows:

$$\mu_f = \Omega\left(\frac{2\gamma_s\sin\theta}{r_f}-\sigma-p_f\right) \quad (3)$$

$$\mu_e = \Omega(K_e\gamma_s-\sigma-p_e) \quad (4)$$

μ_f and μ_e are the face and edge bubble vacancy chemical potentials, respectively. Where K_e is the geometric curvature of the grain edge bubbles and p_f and p_s are the internal gas pressures of face and edge porosity in Pascal, respectively. σ is the external stress in Pascal, Ω is the atomic volume (m^3) and γ_s is the surface tension (J/m^2). r_f is the face bubble radius of curvature and θ is 50° [9]. Using the chemical potential defined above, the rate of production of vacancies on the grain boundary is determined from the observation that the total force acting on a grain face, made up of components from external restraint, capillary force and gas pressure acting on the bubble surfaces, equals the chemical potential per unit volume integrated over the grain face. Other equations described in Ref. [9] for the growth rate of the edge and face bubbles and gas release to the plenum have been adopted in identical form.

2.3. Fuel swelling

The gas bubble swelling has three contributions: intra-granular, grain face and grain edge bubble swelling. The swelling for each group is defined as the bubble concentration multiplied by the bubble volume.

$$S_g = S_{\text{int}} + S_f + S_e \quad (5)$$

The swelling due to cesium is given as 0.47%/at% burnup at low temperatures. However, a significant amount of cesium evaporates

and releases at high temperatures. A balance equation has been adopted to calculate the net swelling per at% burnup based on [9]

$$\frac{dS_{Cs}}{dt} = 5.55 \times 10^{-15} R - 2 \times 10^{-4} \exp\left(-\frac{12280}{T}\right) S_{Cs} \quad (6)$$

S_{Cs} is the Fractional fuel swelling due to cesium, R is the Rating (W/kg), T is the time (s).The first term on the right-hand side of Eq. (6) is cesium production from fission, while the second term represents cesium release. Note that, a fraction of the released cesium can migrate axially under temperature gradient and cause excessive swelling at the fuel blanket interface. This is explained in Section 3.

Swelling due to solid fission products, excluding cesium, is given as 0.19%/at.% burnup [9].

2.4. Isothermal fission gas release benchmarks

The FEAST-OXIDE has been benchmarked against the available experimental UO_2 fission gas release data at 1250, 1500, 1750 and 2000 K and the preliminary OGRES model predictions given in Ref. [9]. In 1980s, such complex simulations were severely limited by the available computational power. OGRES model differential equations were linearized before solving [9]. Such an approach allows for significant gain in computational time but it may also hurt the accuracy of the calculation. In this study, the equations were solved directly in an explicit manner. In addition, some important constitutive relations, such as the diffusion coefficients reported in Ref. [9], were not the latest models suggested by Harwell Institute [13]. Finally, the effect of JOG on fission gas release was not included in the Ref. [9] description. Because of all these differences, OGRES and FEAST predictions do not match well in Figs. 2–5. On the other hand, FEAST predictions are in satisfactory agreement with the experimental data.

Fig. 2 shows that the fuel irradiated at 1250 K has a much higher fission gas release fraction compared to the FEAST model prediction when the effect of JOG formation is neglected. JOG formation starts with the availability of excess oxygen (oxygen-to-metal ratio is above 1.985) around 2 at% burnup. As a consequence, fission gas release increases significantly due to trans-granular fracture and resulting decrease in effective grain size [14]. This behavior is modeled by increasing the fission-enhanced gas diffusion coefficient (Equation-2). In fact the experimental data given in Fig. 2 was used to fit the effect of JOG formation on fission gas release.

3. Fuel chemistry and restructuring

A significant part of the oxide fuel in fast reactors operates at high centerline and surface temperatures, together with a steep temperature gradient. As a consequence, the diffusion of the fuel constituents under the temperature gradient driving force be-

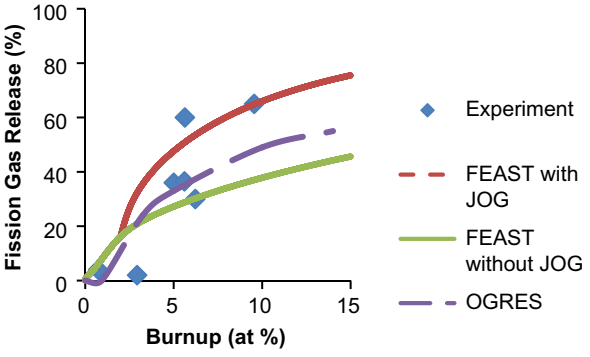

Fig. 2. Fission gas release from fuel irradiated at 1250 K (grain size is 10 μm).

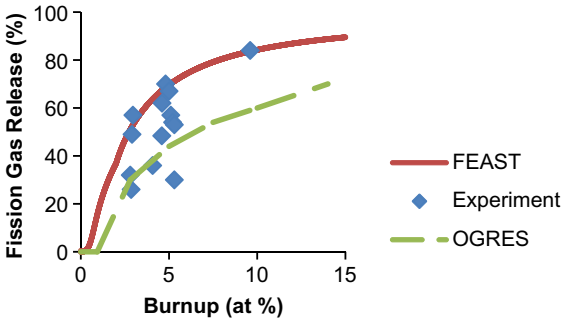

Fig. 3. Fission gas release from the fuel irradiated at 1500 K (grain size is 10 μm).

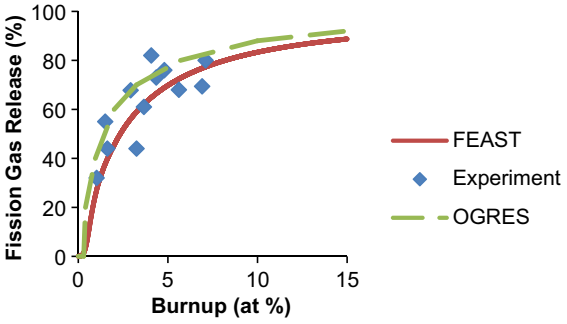

Fig. 4. Fission gas release from the fuel irradiated at 1750 K (grain size is 23 μm).

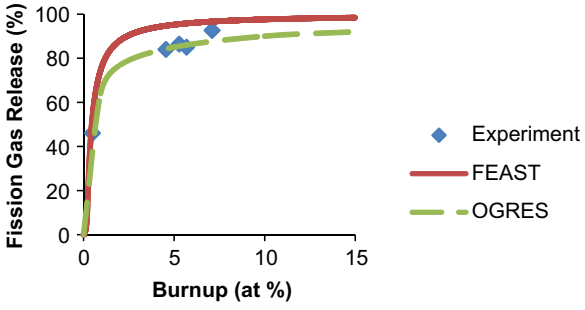

Fig. 5. Fission gas release from the fuel irradiated at 2000 K (grain size is 32 μm).

comes very strong. Typically, the mixed oxide fast reactor fuel is manufactured to be hypo-stoichiometric (i.e., oxygen-to-metal ratio <2) to control the fuel–clad chemical interaction. Predicting the oxygen-to-metal ratio increase with burnup accurately is important for predicting thermal, mechanical and fission gas behavior of the oxide fuel. In FEAST-OXIDE the increase in the oxygen potentials modeled approximately by solving the thermodynamic equilibrium relation between the fuel and fission products and the charge balance within the fuel [16] at each time step and in coupled form. The molybdenum partitioning method is used to assess the equilibrium concentration of the molybdenum within the oxide matrix and within the metallic phase by assuming that molybdenum forms ideal solutions in these phases [16]. When all the plutonium has been oxidized, the oxygen potential decreases for further oxidation. As a consequence, molybdenum gradually transforms from metal to oxide and acts as a buffer to prevent the fuel from becoming hyper-stoichiometric. At high burnup, transformation of a significant amount of molybdenum into the oxide phase may lead to a hyper-stoichiometric fuel.

In addition to the burnup evolution, oxygen tends to redistribute radially under the temperature gradient. The OXIRED model gi-

ven in Ref. [17] is adopted in FEAST-OXIDE. The model is based on the thermo-transport theory (see Appendix). It predicts the oxygen redistribution in the radial direction as a function of time.

It is well-known that uranium and plutonium migrate up the temperature gradient during irradiation, particularly in the radial direction under high temperature gradients [18]. This migration leads to local Pu concentration variations that affect the fuel material properties and power distribution. Hence, the impact on the fuel thermal performance may be considerable. The model applied for actinide migration is again based on the thermo-transport theory (see Appendix). The approach described in Refs. [18,19] is adopted.

Next, radial and axial migration of the cesium and JOG formation will be described.

Cesium plays an important role in fuel pin performance due to its participation in both mechanical and chemical interactions that are potentially life-limiting [20]. Therefore, it is important to develop a detailed understanding of the behavior of cesium in irradiated oxide fuel pins, particularly the mechanism and kinetics of cesium thermo-migration and the mechanism of cesium-oxide fuel reaction swelling.

In high burnup fuel rods, a solid fission product oxide deposit, whose major composition is cesium molybdenate (Cs_2MoO_4), is observed in the gap between the fuel pellet and the cladding. This deposit is called joint oxide gain (JOG); the specific mechanism of its formation is not yet understood [21]. It is known to form when the fuel surface temperature is above 600 °C, the fuel oxygen-to-metal ratio is above 1.985, and the clad temperature is below 600 °C [21]. JOG improves the gap conductance. Due to excessive stresses generated with the diffusion of cesium and molybdenum, localized trans-granular fracture of the fuel, as-fabricated porosity shrinkage and significant release of fission gases were reported in Ref. [14]. Furthermore, Ref. [22] shows that the start of JOG formation and reduction in fission gas retention in the fuel is simultaneous (the increase in fission gas release is due to the reduction in grain size at the brittle part of the fuel). The as-fabricated pore shrinkage and the resulting decrease in fuel swelling are expected to mitigate fuel/clad mechanical interaction (FCMI), while the improvement of the gap conductance reduces fuel centerline temperatures. FEAST-OXIDE conservatively assumes that solid fission product swelling replaces the remaining as-fabricated pores at the locations where JOG forms. The cesium radial migration model is based on the thermo-transport theory as described in [21] (see Appendix). The JOG layer thickness is computed in accordance with the amount of released cesium, which has migrated to the outer region of the fuel pellet assuming the JOG layer density is identical to the fuel density.

In addition to the cesium radial migration and JOG formation, cesium axial migration has a significant impact on the fuel performance. A number of studies on axial cesium migration in mixed oxide fuel pins have shown that cesium migrates down the temperature gradient, resulting in accumulation of cesium and subsequent swelling of cesium compounds at the interface between the core and blanket fuel pellets [20,23–25]. Transport of cesium is based on evaporation/condensation process, and the total flux of cesium, ϕ, across the interface between each axial node can be expressed by the following equation [20]:

$$\phi = k[N(h) - N(c)] \exp\left(-\frac{\Delta H_v}{RT}\right) \tag{7}$$

where $N(h)$ and $N(c)$ are the concentration of cesium on the hotter and cooler side, k is the mobility of cesium vapor (1/s), left as a calibration parameter and found to be equal to 3.5 for best fit with the experimental data base [26–29]. ΔH_v, the partial molar heat of vaporization of cesium, is 177.7 kJ/mol [20], R is the universal gas constant, 8.314 J/mol/K, T is the temperature in Kelvin. The average fuel temperature is to be used in the exponential term. In addition, the axial direction of the cesium current is conservatively specified by the fuel centerline temperature. The cesium vapor reaching the top fuel node is assumed to deposit at the outer radial node and causes swelling. The effect of cesium axial migration on the fuel–clad mechanical interaction and clad straining could be very significant, if the clad does not have good creep strength.

Fuel restructuring includes the migration of as-fabricated porosity and the resulting formation of a central void, grain growth, irradiation-induced densification, fuel cracking and relocation. At power, the pores move to the inner regions of the fuel up the temperature gradient. The as-fabricated porosity migration under the effect of the temperature gradient is described with a vapor transport model. The pore velocity given in Ref. [18] was adopted. The 1D mass continuity equation as described in Ref. [16] is solved to find the time as-fabricated porosity migration in time dependent form. The maximum allowed fuel density at the end of porosity migration process is 97%. A code-to-code benchmark for this process is reported in Section 7. Empirical time dependent models for irradiation-induced densification (Ref. [30]) and grain growth [31] were adopted. Furthermore, an empirical fuel cracking and relocation model given for the JOYO driver fuel in Ref. [32] was taken for FEAST-OXIDE to estimate the gap evolution with a reasonable accuracy.

4. Temperature distribution

Due to its low thermal conductivity, oxide fuel operates with a high temperature gradient in sodium fast reactor operation. Furthermore, the low conductance of the gas filled gap region adds to the fuel centerline temperature. It is obviously very critical to calculate the temperature distribution to estimate the oxide fuel performance. First, fission gas release and gas swelling have a strong dependence on the temperature distribution. Second, as-fabricated pore migration, fuel compressibility, plutonium and oxygen migration are influenced significantly by the temperature distribution. Finally, the cesium evaporation, which affects solid fission product swelling, is also a strong function of temperature. The energy balance method is applied to find the fuel pin temperature distribution. The transient part is modeled with semi-implicit Crank–Nicholson method. Fuel melting and its effect on the mechanical behavior are also included in the model. Eqs. (8) and (9) describe the discretized energy balance equations for a radial node-i before melting and during melting, respectively. ρ is the fuel density, c_p is the specific heat, T is temperature, h_m is the fuel enthalpy, x is the melt fraction, k is the thermal conductivity, q_i''' is the volumetric heat generation rate, A_i is the surface area and r_i is the radial location of node-i.

$$\rho c_p A_i \frac{T_i^{t+1} - T_i^t}{\Delta t} = \frac{1}{2}\left(\frac{T_{i-1}^{t+1} - T_i^{t+1}}{\frac{1}{2\pi k_{i-1,i}}\ln\frac{r_i}{r_{i-1}}} + \frac{T_{i-1}^{t} - T_i^{t}}{\frac{1}{2\pi k_{i-1,i}}\ln\frac{r_i}{r_{i-1}}}\right) + \frac{1}{2}\left(\frac{T_{i+1}^{t+1} - T_i^{t+1}}{\frac{1}{2\pi k_{i+1,i}}\ln\frac{r_{i+1}}{r_i}} + \frac{T_{i+1}^{t} - T_i^{t}}{\frac{1}{2\pi k_{i+1,i}}\ln\frac{r_{i+1}}{r_i}}\right) + q_i''' A_i \tag{8}$$

$$\rho A_i h_m \frac{x_i^{t+1} - x_i^t}{\Delta t} = \frac{1}{2}\left(\frac{T_{i-1}^{t+1} - T_i^{t+1}}{\frac{1}{2\pi k_{i-1,i}}\ln\frac{r_i}{r_{i-1}}} + \frac{T_{i-1}^{t} - T_i^{t}}{\frac{1}{2\pi k_{i-1,i}}\ln\frac{r_i}{r_{i-1}}}\right) + \frac{1}{2}\left(\frac{T_{i+1}^{t+1} - T_i^{t+1}}{\frac{1}{2\pi k_{i+1,i}}\ln\frac{r_{i+1}}{r_i} + \frac{T_{i+1}^{t} - T_i^{t}}{\frac{1}{2\pi k_{i+1,i}}\ln\frac{r_{i+1}}{r_i}}}\right) + q_i''' A_i \tag{9}$$

The single mass velocity model is applied to estimate the coolant axial temperature distribution. The FEAST user is expected to input either the effective subchannel mass flow rate or peak coolant outlet temperature, in addition to the coolant inlet temperature.

The fresh mixed oxide fuel thermal conductivity is adopted from Ref. [14]. It is a recent correlation based on JOYO experimental data. In addition, the correction factors are included to describe the effect of dissolved solid fission products, precipitated solid fis-

sion products, radiation damage and porosity as suggested in [14]. The porosity correction factor is given as follows:

$$F_4 = 1 - \alpha P \tag{10}$$

P is the Fuel Porosity, α is the Porosity factor (1.5 or 2.5 as explained below) In this work, two different values are allowed for the porosity factor, α. Ref. [33] suggests that 1.5 is appropriate for the large pores (above 30 μm) and 2.5 is appropriate for the small pores. For the migration of the as-fabricated porosity during the restructuring period, 1.5 is assumed. After the restructuring period, the as-fabricated porosity decreases due to densification, furthermore, the maximum gas bubble size is on the order of microns. Therefore, 2.5 is assumed conservatively, to calculate the fuel temperature distribution after the restructuring period.

Gap heat transfer is an essential part of thermal modeling of the oxide fuel. High thermal resistance of the gap region may lead to a significant temperature difference between the fuel outer surface and the clad inner surface. On the other hand, the formation of the JOG may improve the thermal resistance significantly. The gap conductance model used in FEAST-OXIDE includes the effects of conduction and radiation heat transfer through the gas (assumed to be helium and xenon), and conduction through the JOG layer. The details can be found in Ref. [6].

5. Fuel–clad chemical interaction

The reaction between uranium–plutonium mixed oxide fuel containing fission products and stainless steel cladding affects the in-reactor fuel performance. Attempts have been made to correlate the depth of attack with the fuel pin operating parameters, chiefly the temperature of the cladding inner surface, the initial O/M ratio of the fuel and the extent of burnup of the fuel [34]. These parameters have been incorporated to a greater or lesser extent into various models and correlations of cladding attack; however, even with their inclusion, these empirical models appear to be of limited applicability. On the other hand, the model given in Refs. [35,36] is better able to reflect the kinetic behavior, O/M ratio of the fuel, cladding temperature and fuel burnup dependency and saturation of the clad wastage; therefore it is adopted in FEAST-OXIDE. The model is based on the data obtained from JOYO and MONJU-type fuel pins irradiated in the Dounreay fast reactor (DFR) and Rapsodie, with supplementary data obtained from pins irradiated in JOYO. The balance equation is based on two stages. In the first stage, the corrodents are released from the fuel; in the second stage, they react with the cladding (see Fig. 6). K_1 is the rate of release of corrodants, C is the quantity of corrodants, K_2 is the rate constant of corrosion reaction, BU is burnup, and t is the time.

It is reported in Ref. [37] that high corrosion rates could be driven by the excess oxygen within the fuel at high burnup and high cladding temperatures (>500 °C). Such type of corrosion mechanisms cannot be predicted by the model given here. In addition, Ref. [38] shows that the accelerated corrosion can be alleviated by using low O/M fuel pellets. Therefore, it is recommended that the FEAST-OXIDE users specify a fuel pin with an initial fuel O/M ratio such that the fuel will not be hyper-stoichiometric for the axial regions in which the clad temperature is above 500 °C.

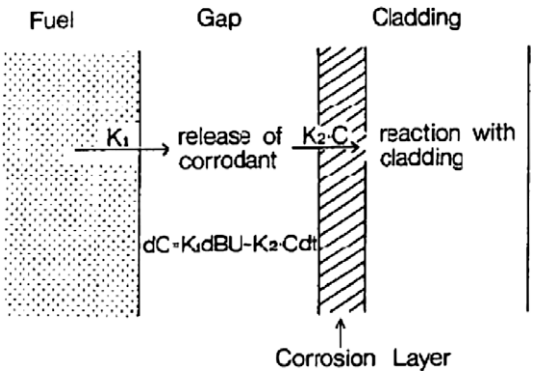

Fig. 6. Fuel–clad chemical interaction Model [36].

6. Mechanical analysis

The first barrier against the release of radioactive fission products into the environment is the cladding of the nuclear fuel rod. The assessment of the cladding stresses and associated deformations is therefore essential in fuel performance calculations. The stress–strain analysis module of FEAST-OXIDE adopts the LIFE algorithm with a 1D finite-difference solution [16].

The model accounts for thermal expansion, elastic, thermal and irradiation creep, plasticity and swelling strains. The code solves the mechanical equilibrium equation with the generalized plain strain approach, by imposing the radial displacement and radial stress are continuous at node interfaces. Furthermore, the axial force balance is also applied to calculate the axial strain (if the gap is open) or the axial frictional force (if the gap is closed). The algorithm assumes the fuel and clad are axially locked once the contact establishes.

The oxide fuel thermal and irradiation creep equations given in Refs. [39,40], respectively, were adopted in FEAST-OXIDE. The plastic behavior of the fuel is modeled with the "perfectly plastic" approach above 1300 °C. As-fabricated porosity shrinkage under the application of an external stress or hot pressing with the dislocation, diffusional and irradiation creep is modeled by the approach suggested in Ref. [16], and thus correlated as a function of creep rate, external stress and the amount of porosity within the fuel. Swelling due to fission gas and solid fission products is received as an input from OGRES calculation.

Fuel cracking and healing model is included in FEAST-OXIDE. Immediately upon startup and before swelling or creep has occurred to any appreciable extent, the fuel develops a network of cracks. Fig. 7 shows the inner plastic region and the cracked outer region. These cracks appear because the thermo-elastic stress com-

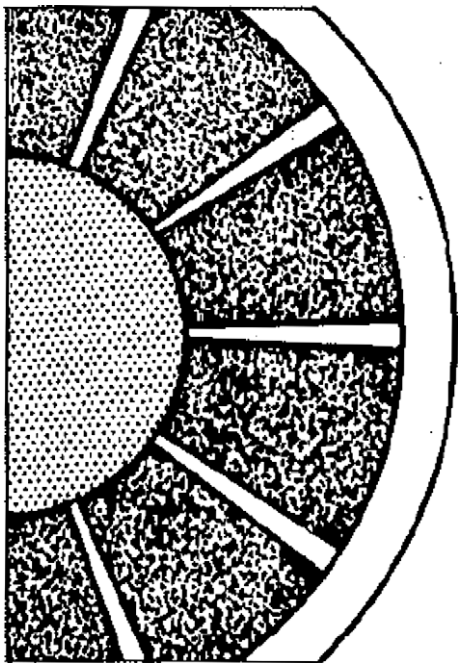

Fig. 7. Cracked mixed oxide fuel pellet and the cladding [41].

ponents exceed the fracture strength of the fuel in tension [16]. When any principal stress exceeds the fracture stress at a fuel radial node below 1300 °C, Young's modulus and Poisson's ratio must be modified as described in Ref. [16], to account for the cracks. When the cracked region of the fuel is under compressive stresses and the temperature is above 1400 °C, the cracks heal and the Young's Modulus and Poisson's Ratio turn back to their original form.

In addition, material properties such as thermal expansion, Young's modulus, Poisson's ratio, yield stress and fracture stress are adopted from MATPRO package [42].

7. Validation of FEAST-OXIDE

7.1. Steady-state

Preliminary benchmarking of the FEAST-OXIDE steady-state capabilities has been accomplished by using Fast Flux Test Facility (FFTF), EBR-II and JOYO experimental data. Clad strain, fission gas release, fuel central void diameter, clad wastage and fuel failure time (breach) have been benchmarked against the experimental data, as well as against LIFE-4 and SIEX fuel performance codes.

7.1.1. FFTF benchmarks

The driver fuel of the FFTF was a mixed oxide fuel. The experimental data for the core demonstration experiment (CDE) lead assemblies [26–29] have been used to benchmark the FEAST-OXIDE code. These assemblies consist of mixed oxide fuel pins with annular pellets. The clad and duct materials are HT 9. The as-fabricated fill gas is at a pressure of 300 kPa. The experimental data reported for the ACO-1 fuel assembly was benchmarked against FEAST-OXIDE [27,28]. Furthermore, LIFE-4, SIEX and FEAST-OXIDE code predictions will be compared for the ACO-3 [26] and CDE [29] fuel assemblies.

7.1.1.1. ACO-1. fuel assembly. Table 1 shows the fuel specifications for the ACO-1 fuel assembly.

Fig. 8 shows that FEAST-OXIDE clad strain predictions match well with the experimental data. Furthermore, FEAST-OXIDE predictions seem to be more conservative in the middle region. This is the peak power region. The low clad strain in the middle region could be due to the JOG formation and resulting excessive pore shrinkage; hence, FEAST seems to err on the conservative side in modeling this phenomenon. High straining of the clad is observed at the top region. First, a significant solid fission product swelling occurs in this region due to cesium axial migration. Second, the operating clad temperature is too high for good HT 9 thermal creep performance. Hence, a moderately high fuel–clad mechanical interaction is enough to strain the cladding. If a more thermal creep-resistant-clad material were to be used (e.g., an ODS), the fuel would have been compressed rather than the clad strained.

Maximum predicted wastage layer is 37 μm at the End of Life (EOL). The experimental data shows that maximum wastage to be 38 μm [27].

Table 1
Fuel specifications for ACO-1 fuel pins.

Property	Value
Clad	HT 9
Fuel pellet density (% of theoretical density)	92.5
Fuel smear density (%)	80
Fuel pellet inner diameter (mm)	1.47
Fuel pellet outer diameter (mm)	5.55
Clad thickness (mm)	0.56
Clad outer diameter (mm)	6.86
Active fuel height (cm)	91.44
Plenum to fuel ratio	1.0
BOL oxygen-to-metal ratio	1.95
Peak linear heat rate (kW/m)	42
Peak subchannel coolant temperature (°C) (BOL)	685
Peak burnup (MWd/kg)/(at%)	123/12.5
Peak fluence ($\times 10^{22}$) (n/cm^2)	19

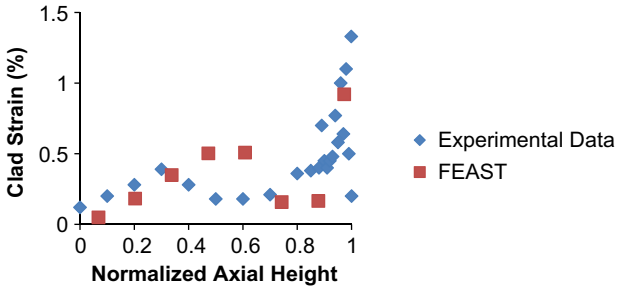

Fig. 8. Comparison of the ACO-1 clad strain data with FEAST-OXIDE.

Table 2
Fuel specifications for ACO-3 fuel pins.

Property	Value
Peak linear heat rate (kW/m)	42.6
Peak subchannel coolant temperature (°C) (BOL)	654
Peak burnup (at%)	16.3
Peak fluence ($\times 10^{22}$) (n/cm^2)	19

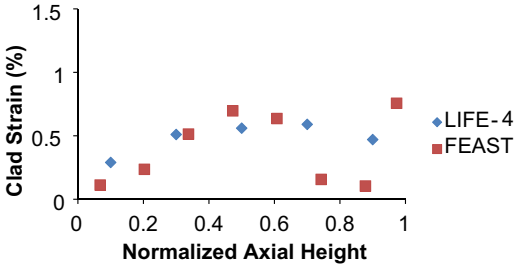

Fig. 9. Comparison of the ACO-3 clad strain predictions between FEAST-OXIDE and LIFE-4 at End of Life.

7.1.1.2. ACO-3. fuel assembly. Table 2 shows the fuel specifications for ACO-3 fuel pins. Note that the geometry and fuel composition of the ACO-3 is the same as ACO-1 but the operating conditions differ. The calculations have been performed with an approximate irradiation history [26,29]. The FEAST-OXIDE and LIFE-4 predictions are compared.

The ACO-3 clad operated with a much lower temperature compared to the ACO-1 clad; hence the clad was more resistant to thermal creep. Fig. 9 shows the clad strain comparison between LIFE-4 and FEAST-OXIDE at the End of Life (EOL). The agreement is reasonable. FEAST appears to be conservative at the critical locations, which are the peak power location (middle) and top of the fuel.

Fig. 10 shows a comparison of the central void diameter predictions of LIFE-4 and FEAST-OXIDE at the End of Life. FEAST-OXIDE somewhat overestimates the void radius at the bottom of the fuel. However, the predictions match well in the middle and upper regions.

7.1.1.3. CDE fuel assembly. The core demonstration experiment (CDE) fuel assembly is one of the most successful mixed oxide fuel assemblies operated in FFTF [27]. LIFE-4 analysis was performed

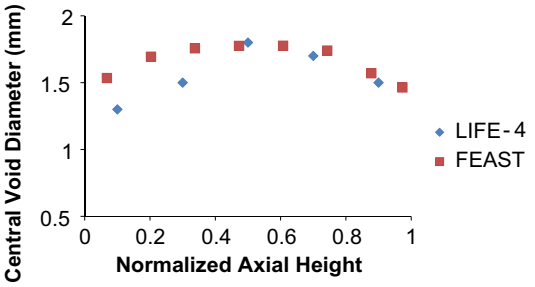

Fig. 10. Comparison of the ACO-3 fuel pin central void diameter predictions between FEAST-OXIDE and LIFE-4 at End of Life.

Table 3
Fuel specifications for CDE fuel pins.

Property	Value
Peak linear heat rate (kW/m)	44.5
Peak subchannel coolant temperature (°C) (beginning of life)	588
Peak burnup (MWd/kg)/(at%)	168/17.1
Peak fluence ($\times 10^{22}$) (n/cm^2)	25.6

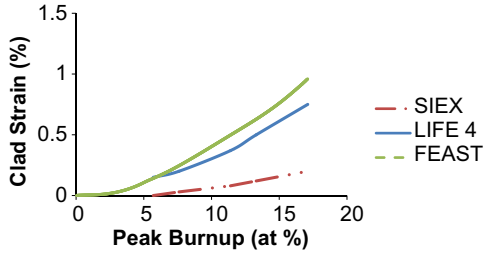

Fig. 11. Comparison of the clad strain predictions between LIFE-4, SIEX and FEAST-OXIDE.

up to 17.1 at%. Similarly, FEAST-OXIDE analysis has been performed up to 17.1 at% and comparisons have been made. Fuel specifications for the CDE fuel pin are given in Table 3.

The cladding of the CDE fuel pin operated at lower temperatures than the ACO-1 and ACO-3 cases; hence, the clad strain remained low in the top region, up to the end of the simulation. The critical location is the middle region. Due to increased contact pressure, clad straining occurs. Fig. 11 shows a comparison of the clad strain predictions by different codes. The version of SIEX given in [29] does not account for the fuel–clad mechanical interaction; hence, it significantly underestimates the clad strain. FEAST-OXIDE lies on the conservative side compared to LIFE-4 and SIEX code predictions.

7.1.2. EBR-II benchmarks

The breached fuel pins operated in the P42R test in EBR-II were benchmarked against FEAST-OXIDE [43]. These fuel pins possessed a high smear density, high linear heat rates and a thinner clad. The fuel specifications, the burnup at which the breaches were observed, and the FEAST-OXIDE predictions are given in Table 4. The experimental data for the time to failure for 316 SS given in Ref. [44] as a function of hoop stress and temperature were used to predict the time of failure.

As can be seen in Table 4, the Sample-3 failure burnup is somewhat overestimated and the Sample-1 and Sample-2 failure burnups are well predicted.

Table 4
EBR-II high smear density fuel specifications.

Property	Sample-1	Sample-2	Sample-3
Fuel smear density (%)	92.3	92.3	92.3
Fuel pellet as-fabricated porosity (%)	6.6	6.6	6.6
Clad material	316SS	316SS	316SS
Clad thickness (mm)	0.28	0.28	0.28
Clad outer diameter (mm)	6.86	6.86	6.86
Active fuel height (cm)	34.3	34.3	34.3
Plenum to fuel ratio	1.0	1.0	1.0
Oxygen-to-metal ratio	1.945	1.916	1.916
Peak linear heat rate (kW/m)	40.4	45.6	47.3
Peak clad temperature (°C)	574.0	621.0	560.0
Peak fluence ($\times 10^{22}$)	3.7	2.1	2.2
Peak burnup at rupture (at%)	3.9	2.5	1.8
FEAST prediction (at%)	3.9	2.6	2.5

Table 5
JOYO MK-1 and MK-II fuel specifications.

Property	MK-I	MK-II
Pellet diameter (mm)	5.4	4.63
Pellet density (%)	93.5	93.0
Wire diameter (mm)	1.2	0.9
Clad material	316SS	316SS
Clad thickness (mm)	0.35	0.35
Clad outer diameter (mm)	6.3	5.5
Plenum to fuel ratio	1.0	1.0
Active core height (m)	0.6	0.55
Oxygen-to-metal ratio	1.98	1.98
Peak linear heat rate (kW/m)	32	40
Reactor coolant inlet temperature (°C)	370	370
Peak coolant exit temperature (°C)	470.0	500.0
Peak flux (n/cm^2/s)	3E+15	5.1E+15
Maximum average burnup (MWd/kg)/(at%)	42/4.3	50/5.1

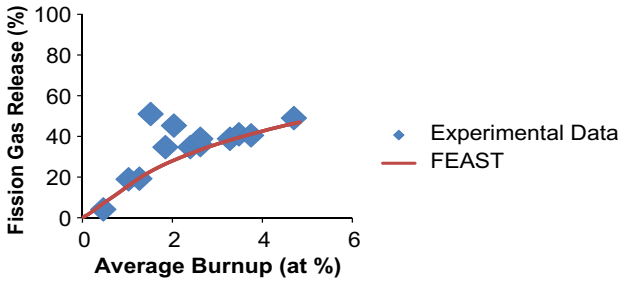

Fig. 12. Fission gas release behavior of MK-I type fuel.

7.1.3. JOYO benchmarks

The MK-I and MK-II fuel specifications operated in JOYO are given in Table 5 [45]. The experimental fission gas release data reported in Ref. [45] were used to benchmark with FEAST-OXIDE.

Comparison of the experimental fission gas release data for MK-I and MK-II are given in Figs. 12 and 13, respectively.

7.2. Transients

A slow-ramp extended over-power test was conducted in EBR-II for mixed oxide fuel pins [46]. Table 6 shows the fuel specifications. The clad materials are the modified austenitic stainless steels D9 and SUS-316 [46]. The initial conditions prior to the transient scenario for each fuel pin are given in Table 7. The reactor power linearly increased from 38.5 MWt to 73.3 MWt. The scenario was simulated with FEAST-OXIDE and its predictions benchmarked against the experimental data.

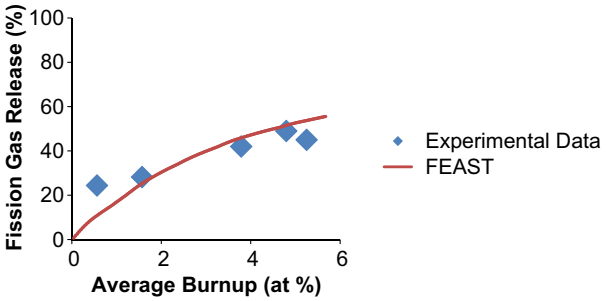

Fig. 13. Fission gas release behavior of MK-II type fuel.

The analysis has been accomplished assuming fuel and clad are locked to each other, if the fuel is constrained by the cladding. It is stated in Ref. [46] that few fuel pins show significant elongation axially; whereas others remain axially constrained by the clad. Significant axial elongation may occur due to the transverse fuel cracking and lifting of the fuel with the molten part. Neglecting these effects and assuming the fuel and clad are axially locked is a conservative assumption. After the steady-state operation, the reactor operating conditions were adjusted at a different level than the End of Life condition and the reactor was operated with the new conditions approximately for a week period prior to the transient initiation. This period is called pre-conditioning.

The temperature distribution, contact pressure and transient clad strain variation are depicted in Figs. 14–16 for the WT 180 fuel element, as a representative example. Fig. 14 shows that 37% of the peak power fuel pellet (by area) is molten at the end of the transient. The Ref. [46] reports 32% areal melt, which is consistent with FEAST-OXIDE predictions.

Fig. 15 shows the variation of the contact pressure and the plenum pressure during the transient at the top position of the fuel pin. The contact pressure first rises up to 400 s due mainly to the thermal expansion of the fuel. When the clad temperature is high enough for thermal creep straining (Fig. 16), the contact pressure is relieved. Furthermore, there are some spikes appearing in Fig. 15, which are due to the activation of the NEFIG intra-granular gas model. If a fuel radial node exceeds 1800 °C, NEFIG model is activated to describe the rapid coarsening of the intra-granular gas bubbles and the gas release. Hence, the spikes are due to rapid swelling of the intra-granular gas bubbles.

Table 8 shows that no failure has been detected for this fuel pin, in spite of partial fuel melting. This is due to the accommodation of molten fuel in the central void, which prevents excessive FCMI. Similarly, FEAST-OXIDE predictions show no failure. Typically, the CDF remains below 0.3. Fuel pins tested with a transient peak power around 60 kW/m such as WT 028, WT 022, WT 033 and WT 011 show small cladding strain. The FEAST predictions are consistent with this behavior. The WT 118 fuel pin also has a transient peak at 60 kW/m but a higher transient clad strain occurs. Note

Table 7
Initial and final conditions during the over-power transient.

Test element	Pre-conditionining (peak power (kW/m)	Pre-conditioning peak clad temperature (°C)	Transient peak power (kW/m)	Transient peak clad temperature (°C)
WT 028	33.6	577	63.9	766
WT 118	31.7	641	60.3	885
WT 107	38.8	617	73.9	841
WT 022	30.8	594	58.7	797
WT 033	31.6	574	60.1	759
WT 180	39.4	624	75.0	853
WT 179	39.1	622	74.4	850
WT 011	30.7	625	58.5	856

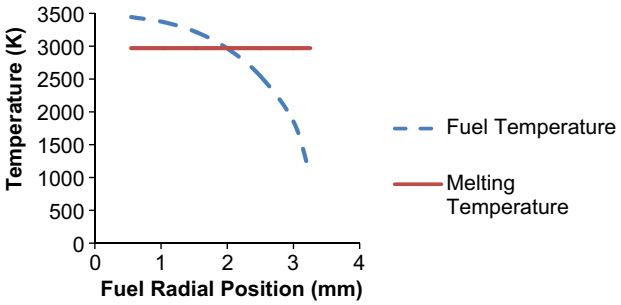

Fig. 14. Peak fuel temperature for the WT 180 fuel pin at 910 s (end of the transient).

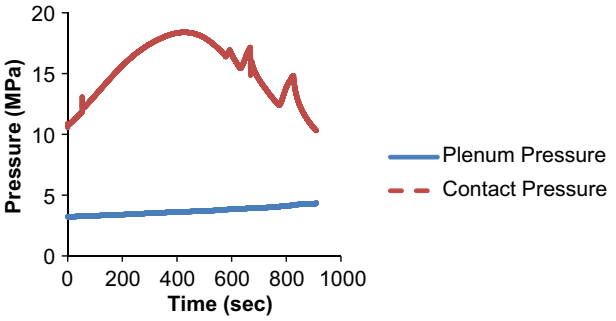

Fig. 15. The variation of the contact pressure at the top node (WT 180 fuel pin).

Table 6
Fuel specifications for TOP-1D test elements.

Test element	Time averaged clad ID temperature (prior to transient) (°C)	EOL* peak power (kW/m)	Peak burnup (at%)	Clad OD** (mm)	Pellet density (% TD***)	Pellet diameter (mm)	Smear density (% TD)	Fuel O/M	Pu content (wt%)	Plenum to fuel ratio
WT 028	630	35.0	2.5	6.985	90.4	6.166	88.0	1.95	22.5	1.12
WT 118	650	34.7	9.3	5.842	93.4	4.996	90.3	1.96	33.0	1.18
WT 107	640	42.4	7.7	6.985	92.9	6.149	90.0	1.97	22.5	1.12
WT 022	600	31.8	6.0	6.985	90.3	6.093	85.9	1.95	30.0	1.12
WT 033	600	33.1	5.9	6.985	90.4	6.165	88.0	1.95	30.0	1.12
WT 180	635	37.6	6.9	6.985	94.6	6.162	89.7	1.97	22.5	1.12
WT 179	650	39.0	7.1	6.985	94.6	6.162	89.7	1.97	22.5	1.12
WT 011	610	34.6	6.4	6.985	90.3	6.093	85.9	1.95	22.5	1.12

* End of Life.
** Outer diameter.
*** Theoretical density.

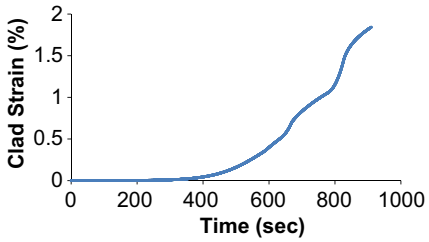

Fig. 16. The increase in transient cladding strain (WT 180 fuel pin).

Table 8
Comparison of the results with FEAST-OXIDE.

Test element	Transient clad strain (experimental data) (%)	Transient clad strain (FEAST-OXIDE)	Axial location (X/L^*)	Failure time (experimental data)	Failure time (FEAST-OXIDE)
WT 028	0.15	0.0	0.8	No failure	No failure
WT 118	0.25	0.8	1.0		
WT 107	0.10	0.36	1.0		
WT 022	0.00	0.0	–		
WT 033	0.06	0.07	0.9		
WT 180	1.50	1.80	1.0		
WT 179	0.70	1.40	1.0		
WT 011	0.07	0.0	0.7		

* Relative position along the axial length of the fuel rod.

that this fuel pin has a much higher burnup, its smear density is higher and the initial porosity (or central void diameter) is lower than the WT 028, WT 022, WT 033 and WT 011 cases. The experimental data shows that the magnitude of clad strain is somewhat higher. The FEAST-OXIDE clad strain prediction is also higher and somewhat on the conservative side.

The WT 107, WT 179 and WT 180 fuel pins were operated with a higher peak transient over-power (75 kW/m) compared to the other fuel pins. The WT 107 clad strain is much lower compared to WT 179 and WT 180, although the transient history is similar, because the initial porosity, or the central void diameter of WT 107 is much larger; hence there is more space for accommodation of the expansion of the molten fuel. The WT 179 and WT 180 fuel pins have a low initial as-fabricated porosity and central void diameter. As a consequence, melting of the fuel causes much higher straining of the clad in these cases. Note that the FEAST-OXIDE predictions are again reasonably good and on the conservative side.

Transient fission gas release experimental data show that low burnup fuel elements have 10–20% fission gas release during the transient. The FEAST-OXIDE prediction for WT 028 fuel element is 17%, hence, it is consistent with the experimental data. The fission gas release for the high burnup fuel elements are reported as much smaller [46]. The FEAST-OXIDE predictions for the higher burnup fuel are of the order of 5%; hence, the code is also consistent with the experimental data.

8. Conclusions

A new computer code, FEAST-OXIDE, was developed to predict the steady and transient behavior of mixed oxide fuels in sodium fast reactors. Attractive/novel features of FEAST-OXIDE with respect to other oxide-fuel codes include a flexible structure that allows for easy integration of constitutive models for new metal fuel alloys and clad materials, the ability to account for the variation of material properties (fuel creep, thermal expansion, Young's modulus) with the local composition present, a mechanistic fission gas release and swelling model originally developed based on the vacancy flow and including the effects of the JOG formation, a detailed fuelchemistry model, cladding wastage model with a better kinetics description.

The steady-state part of FEAST-OXIDE was benchmarked against the available FFTF, EBR-II and JOYO database. Furthermore, the code's transient capabilities were benchmarked against the EBR-II slow-ramp overpower tests. Seven steady-state cases and eight transients were simulated. The steady-state cases correspond to burnup between 2 and 17 at%; whereas the transient analyses span the range between 2 and 9 at%. The peak clad temperature for the steady-state simulations varies between 550 °C and 700 °C, while it is between 760 °C and 860 °C for the transient simulations. The peak cladding dose was 125 dpa. The agreement for all these benchmarks was satisfactory.

Acknowledgements

This project is supported by Nuclear Regulatory Commission. The authors would like to thank to Professor Mujid S. Kazimi for many fruitful discussions.

Appendix A

The appendix describes the thermal diffusion algorithm used for oxygen, actinides and cesium radial redistribution within the fuel.

The net current is defined as a function of temperature gradient and concentration gradient as follows:

$$J = -D\left(\nabla c + c\frac{Q}{RT^2}\nabla T\right)$$

Q is the molar effective heat of transport (J/mol), T is the fuel temperature (K), R is the gas constant = 8.314 J/mol/K (or 1.987 cal/mol/K), D is the diffusion coefficient of the fuel constituent of interest (m^2/s), c is the concentration of the diffusing species (mol), J is the current ($mol/m^2/s$)

The equation of continuity is:

$$\frac{\partial c}{\partial t} = -\nabla \cdot J \tag{A.1}$$

The finite-difference discretization of Eq. (A.1) gives the following relation:

$$c_t^i = c_{t-1}^i + 2\Delta t\frac{J_+^{i-1}\times rc^{i-1} - J_+^i \times rc^i + J_-^i \times rc^i - J_-^{i+1}\times rc^{i+1}}{(r_i^2 - r_{i-1}^2)} \tag{A.2}$$

rc^i is the center of node-i (m), r_i is the outer boundary of node-i (m), J_+^i is the positive oxygen current emerging from node-i towards the outer part of the fuel. Its sign is positive ($atom/m^2/s$), J_-^i is the negative oxygen current emerging from node-i towards the inner part of the fuel. Its sign is negative ($atom/m^2/s$).

A.1. Diffusion coefficients

Oxygen diffusion coefficient (m^2/s):

$$D_O = 1.39\times 10^{-6}\times \exp\left(-\frac{9128}{T}\right)$$

T is the temperature (K).

Plutonium diffusion coefficient (m^2/s):

$$D_{Pu} = 0.34\times 10^{-4}\times \exp\left(-\frac{55351}{T}\right)$$

T is the temperature (K).

Cesium diffusion coefficient (m^2/s):

$$D_{Cs} = D_1 + D_2 + D_3$$

$$D_1 = 7.6 \times 10^{-10} \exp\left[-\frac{6.95 \times 10^4}{RT}\right]$$

$$D_2 = S^2 J_v c_v^0$$

$$J_v = 10^{13} \exp\left(-\frac{5.48 \times 10^4}{RT}\right)$$

$$c_v^0 = \frac{\alpha_s S^2 + ZV_0}{2Z} \times \left[\sqrt{1 + \frac{4KZ}{J_v(\alpha S^2 + ZV_o)}} - 1\right]$$

α_s is the sink intensity, Z is the number of sites surrounding a defect (=2), K is the generation rate of defects (=E+4), S is the 3.45E−10 m, R is the 1.987 cal/mol/K, T is the temperature (K).

$$V_o = \exp\left(-\frac{5.52 \times 10^4}{RT}\right)$$

$$D_3 = 2 \times 10^{-40} F$$

where F is the fission rate in fissions/m^3/s.

A.2. Heat of transports

Oxygen heat of transport (J/mol) is given as a function of the charge of plutonium (V_{pu}) and the charge of Uranium (V_u):

$$Q_o = \begin{cases} -8.12 \times 10^{-4} \exp(4.85 V_{Pu}) & V_{Pu} < 3.3 \\ -3.96 \times 10^{-6} + 2.37 \times 10^6 V_{Pu} - 3.6 \times 10^5 V_{Pu}^2 & 3.3 \le V_{Pu} < 4.0 \\ -3.5 \times 10^{34} \exp(-17 V_U) & V_U \ge 4.0 \end{cases}$$

Plutonium heat of transport (cal/mol):

$$Q_{Pu} = 35000$$

Cesium heat of transport (cal/mol):

$$Q_{Cs} = 60000$$

A.3. Boundary conditions

$$J_+(R_o) = 0$$
$$J_-(0) = 0$$

R_o is the outer radius of the fuel pellet (m).

References

[1] US DOE Nuclear Energy Research Advisory Committee and the Generation IV International Forum, A Technology Roadmap for Generation IV Nuclear Energy Systems, US Department of Energy, Report, December 2002.
[2] US Department of Energy, Global Nuclear Energy Partnership Strategic Plan, US Department of Energy, Report No. GNEP-167312, Rev. 0, 2007.
[3] B. Cohen, H. Tsai, L.A. Neimark, Journal of Nuclear Materials 204 (1993) 244.
[4] Y. de Carlan, J.L. Bechade, P. Dubuisson, J.L. Seran, P. Billot, A. Bougault, T. Cozzika, S. Doriot, D. Hamon, J. Henry, M. Ratti, N. Lochet, D. Nunes, P. Olier, T. Leblond, M.H. Mathon, Journal of Nuclear Materials 386 (2009) 430.
[5] S.C. Chapra, R.P. Canale, Numerical Methods for Engineers, McGraw-Hill International Editions, 1998.
[6] A. Karahan, J. Buongiorno, M.S. Kazimi, Modeling of Thermo-Mechanical and Irradiation Behavior of Metallic and Oxide Fuels for Sodium Fast Reactors, Report No: MIT-NFC-TR-110, Center for Advanced Nuclear Energy Systems, Massachusetts Institute of Technology, 2009.
[7] M.H. Wood, J.R. Matthews, Journal of Nuclear Materials 91 (1980) 35.
[8] H. Wood, J.R. Matthews, Journal of Nuclear Materials 102 (1981) 223.
[9] M.H. Wood, J.R. Matthews, Journal of Nuclear Materials 91 (1980) 241.
[10] M.H. Wood, J.R. Matthews, H.R. Matthews, Journal of Nuclear Materials 87 (1979) 167.
[11] R.I. Brearley, D.A. MacLnnes, Journal of Nuclear Materials 95 (1980) 239.
[12] A.H. Booth, A Method of Calculating Fission Gas Diffusion from UO_2 Fuel and its Application to the X-2-f Loop Test, Report AECL 496, 1957.
[13] M.H. Wood, J.R. Matthews, F.A. Johnson, A.J. Walter, Journal of Nuclear Materials 92 (1980) 354.
[14] M. Inoue, K. Maeda, K. Katsuyama, K. Tanaka, K. Mondo, M. Hisada, Journal of Nuclear Materials 326 (2004) 59.
[15] J.R. Matthews, M.H. Wood, European Applied Research Report – Nuclear Science Technology 5 (1984) 1685.
[16] D.R. Olander, Fundamental Aspects of Nuclear Reactor Fuel Elements, US DOE, 1976.
[17] K. Lassmann, Journal of Nuclear Materials 150 (1987) 10.
[18] C.F. Clement, M.W. Finnis, Journal of Nuclear Materials 75 (1978) 193.
[19] T. Ishii, T. Asaga, Journal of Nuclear Materials 294 (2001) 13.
[20] H. Furuya, S. Ukai, S. Shikakura, Y. Tsuchiuchi, K. Idemitsu, Axial distribution of cesium in heterogeneous FBR fuel pins, Journal of Nuclear Materials 201, 1993, pp. 46–53.
[21] T. Ozawa, T. Abe, Nuclear Technology 156 (2006) 39.
[22] J.C. Melis, Journal of Nuclear Materials 204 (1993) 188.
[23] M.G. Adamson, S. Vaidyanathan, Transactions of American Nuclear Society 38 (1981) 289.
[24] S. Vaidyanathan, M.G. Adamson, Transactions of American Nuclear Society 38 (1981) 291.
[25] R.A. Karnesky, J.W. Jost, I.Z. Stone, cesium migration in LMFBR fuel pins, in: International Conference on Fast Breeder Reactor Fuel Performance, Monterey, California, 1979.
[26] A. Biancheria, T.S. Roth, B.E. Sundquist, Steady-state and transient fuel pin performance modeling: LIFE-4 update, in: International Conference on Reliable Fuels for Liquid Metal Reactors, American Nuclear Society, Arizona, 1986, pp. 5.1–5.14.
[27] A.E. Bridges et al., Advanced Liquid Metal Reactor Fuel and Blanket Designs Using HT 9, WHC-SA—1073, Westinghouse Hanford Co., Richland, WA, 1991.
[28] R.B. Baker et al., Performance of Fast Flux Test Facility Driver and Prototype Driver Fuels, WHC-SA—0974, Westinghouse Hanford Co., Richland, WA, 1990.
[29] A.J. Lovell et al., Demonstration of a high burnup heterogeneous core using ferritic/martensitic materials, in: International Conference on Reliable Fuels for Liquid Metal Reactors, ANS, 1986.
[30] H. Többe, IAMBUS: A Computer Code for the Design and Performance Prediction of Fast Breeder Fuel Rods, Technical Report, DE03FH121, Bergisch Gladbach 1, May, 1990.
[31] C. Sari, Journal of Nuclear Materials 137 (1986) 100.
[32] M. Inoue, K. Yamamoto, T. Sekine, M. Osaka, N. Kushida, T. Asaga, Journal of Nuclear Materials 323 (2003) 108.
[33] M. Inoue, K. Abe, I. Sato, Journal of Nuclear Materials 281 (2000) 117.
[34] L.A. Lawrence, Nuclear Technology 64 (1984) 139.
[35] K. Konashi, N. Nakae, K. Kamimura, Y. Yokouchi, J. Komatsu, Nuclear Technology 72 (1985) 328.
[36] K. Konashi, N. Nakae, K. Kamimura, Y. Yokouchi, J. Komatsu, Model Analysis of Fuel Cladding Chemical Interaction, Nuclear Fuel Performance, British Nuclear Energy Society, London, 1985. pp. 43–46.
[37] P. Martin, M. Pelletier, E. Denis, D. Buckthorpe, Nuclear Technology 161 (2008) 35.
[38] H. Kashihara, S. Shikakura, Y. Yokouchi, I. Shibahara, H. Matsushima, K. Yamamoto, Dimensional Stability of FBR Fuel Pins with Modified Type 316 Stainless Steel Cladding at High Burnup, Fast Reactor Core and Fuel Structural Behavior, British Nuclear Energy Society, London 1985, pp. 243–247.
[39] J.L. Routbort, Journal of Nuclear Materials 44 (1972) 247.
[40] P. Combette, C. Milet, G. Tanis, J. Crouzet, M. Masson, Journal of Nuclear Materials 65 (1977) 37.
[41] P. Verbeek, H. Többe, N. Hoppe, B. Steinmetz, Nuclear Technology 39 (1978) 167.
[42] C.M. Allison, G.A. Berna, R. Chambers, E.W. Coryell, K.L. Davis, D.L. Hagrman, D.T. Hagrman, N.L. Hampton, J.K. Hohorst, R.E. Mason, M.L. McComas, K.A. McNeil, R.L. Miller, C.S. Olsen, G.A. Reymann, L.J. Siefken, SCDAP/RELAP5/MOD3.1 Code Manual Volume IV: MATPRO – A Library of Materials Properties for Light-Water-Reactor Accident Analysis, NUREG/CR-6150, 1993.
[43] L.A. Lawrence, S.M. Jensen, J.W. Hales, R.A. Karnesky, B.J. Makenas, performance of advanced oxide fuel pins in EBR-II, in: International Conference on Reliable Fuels for Liquid Metal Reactors, ANS, 1986.
[44] R.J. Puigh, M.L. Hamilton, In-reactor creep rupture behavior of the D9 alloys, in: CONF-860605—44, Hanford Engineering Development Lab, Richland, WA, June, 1986.
[45] T. Shimada, T. Itaki, Y. Nara, J. Komatsu, Operational experience of experimental fast reactor JOYO driver fuel, in: International Conference on Reliable Fuels for Liquid Metal Reactors, ANS, 1986.
[46] H. Tsai, L.A. Neimark, T. Asaga, S. Shikakura, Journal of Nuclear Materials 204 (1993) 217.